Cell Reports

Article

Subiculum as a generator of sharp wave-ripples in the rodent hippocampus

Graphical abstract

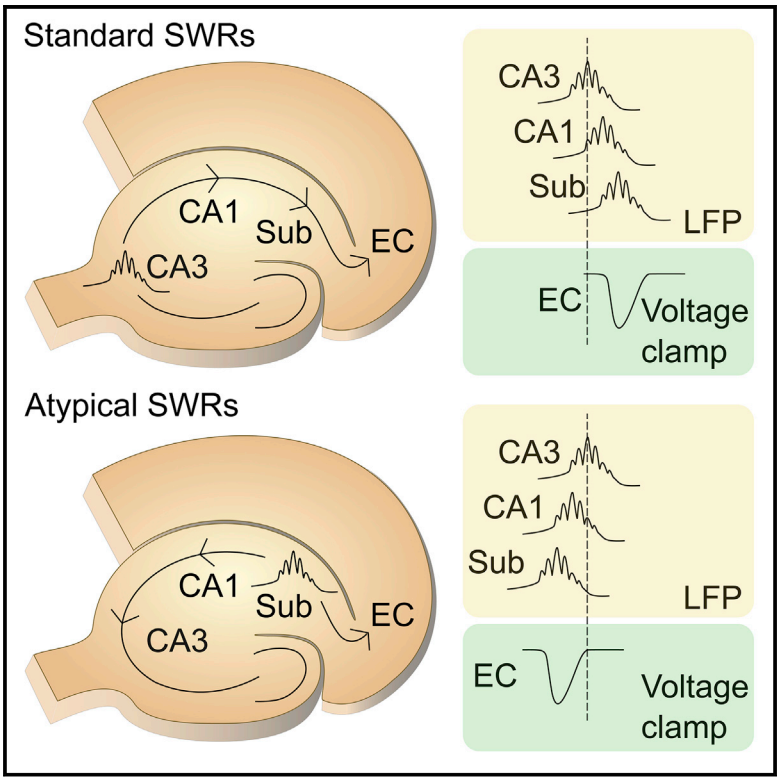

Highlights

- A fraction of sharp wave-ripples does not rely on CA2/3 generation
- The subiculum can work as independent generator for sharp wave-ripples
- These events can propagate back from the subiculum into CA1 and CA3

Authors

Barbara Imbrosci, Noam Nitzan, Sam McKenzie, ..., Claudia Böhm, Nikolaus Maier, Dietmar Schmitz

Correspondence

dschmitz-office@charite.de

In brief

Imbrosci et al. show that the subiculum can work as a secondary generator of sharp wave-ripples (SWRs). SWRs with their origin in subiculum can propagate to the entorhinal cortex and backward to CA1 and CA3.

Imbrosci et al., 2021, Cell Reports *35*, 109021
April 20, 2021
https://doi.org/10.1016/j.celrep.2021.109021

CellPress

Cell Reports

CellPress
OPEN ACCESS

Article

Subiculum as a generator of sharp wave-ripples in the rodent hippocampus

Barbara Imbrosci,[1,2] Noam Nitzan,[2,9] Sam McKenzie,[7,10] José R. Donoso,[2,4,11] Aarti Swaminathan,[2] Claudia Böhm,[2,12] Nikolaus Maier,[2,8] and Dietmar Schmitz[1,2,3,4,5,6,8,13,*]

[1]German Center for Neurodegenerative Diseases (DZNE) Berlin, 10117 Berlin, Germany
[2]Charité – Universitätsmedizin Berlin, corporate member of Freie Universität Berlin and Humboldt-Universität zu Berlin, and Berlin Institute of Health, Charitéplatz 1, 10117 Berlin, Germany
[3]NeuroCure Cluster of Excellence, Charitéplatz 1, 10117 Berlin, Germany
[4]Bernstein Center for Computational Neuroscience (BCCN) Berlin, 10115 Berlin, Germany
[5]Einstein Center for Neurosciences (ECN) Berlin, 10117 Berlin, Germany
[6]Max-Delbrück-Centrum (MDC) for Molecular Medicine, 13125 Berlin, Germany
[7]Neuroscience Institute, New York University, New York, NY 10016, USA
[8]These authors contributed equally
[9]Present address: Neuroscience Institute, New York University, New York, NY 10016, USA
[10]Present address: Department of Neurosciences, University of New Mexico, Albuquerque, NM, USA
[11]Present address: Institute for Neural Computation, Ruhr-Universität Bochum, 44801 Bochum, Germany
[12]Present address: Howard Hughes Medical Institute, Janelia Research Campus, Ashburn, VA 20147, USA
[13]Lead contact
*Correspondence: dschmitz-office@charite.de
https://doi.org/10.1016/j.celrep.2021.109021

SUMMARY

Sharp wave-ripples (SWRs) represent synchronous discharges of hippocampal neurons and are believed to play a major role in memory consolidation. A large body of evidence suggests that SWRs are exclusively generated in the CA3-CA2 network. In contrast, here, we provide several lines of evidence showing that the subiculum can function as a secondary SWRs generator. SWRs with subicular origin propagate forward into the entorhinal cortex as well as backward into the hippocampus proper. Our findings suggest that the output structures of the hippocampus are not only passively facilitating the transfer of SWRs to the cortex, but they also can actively contribute to the genesis of SWRs. We hypothesize that SWRs with a subicular origin may be important for the consolidation of information conveyed to the hippocampus via the temporoammonic pathway.

INTRODUCTION

Learning and memory requires a constant interchange of information between cortical and hippocampal networks (Buzsáki, 1989). According to the two-stage model of memory trace formation, during alert wakefulness, the hippocampus receives and encodes highly processed information from the neocortex. In this first stage, the new memory traces stored in the hippocampal network are labile. A second stage, occurring during subsequent resting periods, seems to be essential for their stabilization and permanent storage (Buzsáki, 1998). During these "offline" brain states, the consolidation of the recently acquired memory traces is believed to be mediated by hippocampal sharp waves and associated ripples (sharp wave-ripple complexes [SWRs]) (Wilson and McNaughton, 1994; Girardeau and Zugaro, 2011; Csicsvari and Dupret, 2013). The pivotal role of SWRs in the process of memory consolidation is supported by studies showing that SWRs can replay neuronal activity that which contain information about recent active behavior (Kudrimoti et al.,1999; Nádasdy et al., 1999; Lee and Wilson, 2002). Furthermore, the experimental suppression of SWRs has been shown to influence the acquisition of new memories (Girardeau et al., 2009; Ego-Stengel and Wilson, 2010; Fernández-Ruiz et al., 2019). SWRs represent highly synchronous population discharges that dominate the hippocampal networks during slow wave sleep (SWS), quiet wakefulness, and consummatory behaviors (Buzsáki, 1986; Chrobak and Buzsáki, 1996). They are generated in the hippocampus and can emerge even in the absence of extra-hippocampal inputs (Bragin et al., 1995). From the site of origin, SWRs travel across the hippocampal CA3 and CA1 subfields, through the subiculum and retrohippocampal structures (Chrobak and Buzsáki, 1994; Böhm et al., 2015) toward cortical targets (Chrobak and Buzsáki, 1996; Siapas and Wilson, 1998; Wierzynski et al., 2009). Given their propensity to propagate, they have been proposed to serve as carriers to transfer recently acquired memory traces from the hippocampus to neocortical locations for long-term storage (Buzsáki, 2015; Khodagholy et al., 2017).

There is a strong consensus that the buildup of excitability leading to the genesis of SWRs occurs in the highly recurrent CA3 network (Buzsáki, 1986, 1989; Csicsvari et al., 2000), with a possible contribution, during waking periods, of the

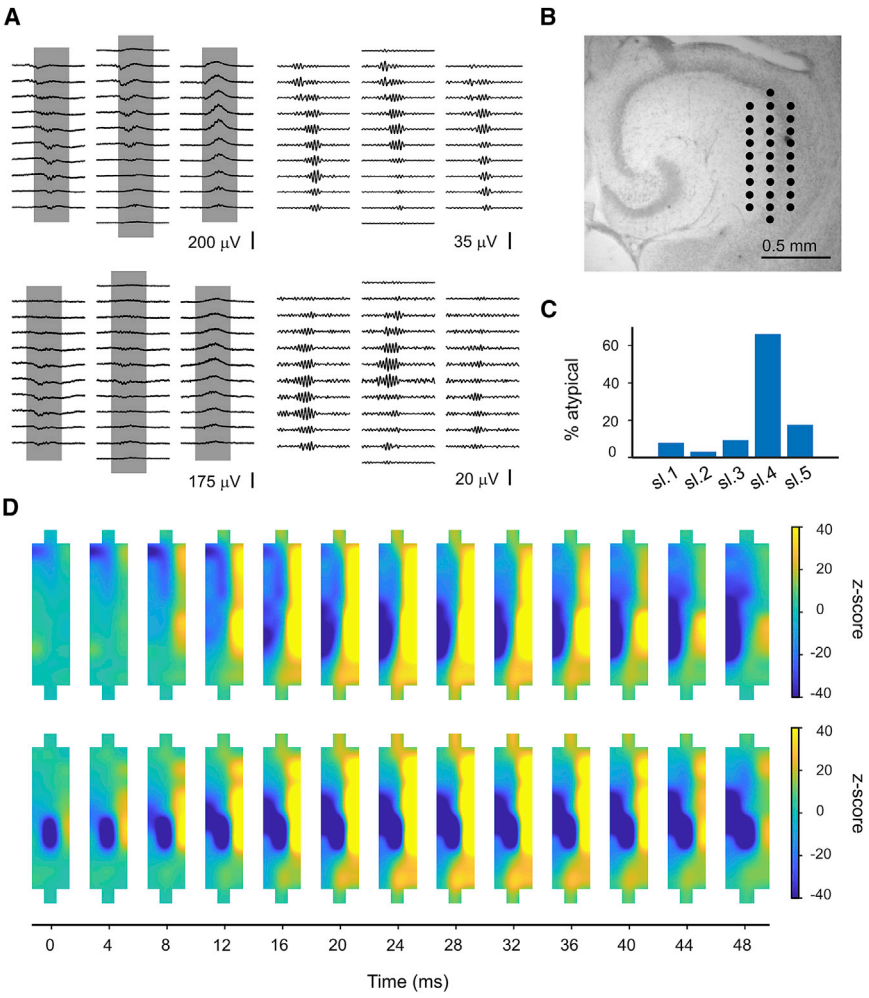

Figure 1. Multi-channel recordings reveal an atypical site of SWR origin

(A) Representative, 100-ms-long, raw (left) and ripple-filtered (150–300 Hz) (right) signals from the 32 perforated MEA (pMEA) channels showing an SWR event with a standard (top) and an atypical (bottom) propagation.

(B) Nissl staining of the hippocampal slice from which the pMEA recordings in (A) were performed. The schematic drawings represent the location of the 32 electrodes of the pMEA.

(C) Percentage of SWRs with an atypical origin and propagation in different slices.

(D) Pseudocolor maps representing the amplitude *Z* scores of the SWR voltage deflections shown in (A). Each plot represents a 4-ms time frame. Displayed data correspond to the signal within the gray shading boxes in (A). On top, the population activity first arises in channels covering the proximal CA1 and displays positive/negative voltages presumably reflecting Schaffer collateral-associated input from CA3, before propagating toward distal CA1 and the subiculum. On the bottom, the population activity first arises in distal CA1 and then propagates bidirectionally, toward proximal CA1 and the subiculum.

neighboring CA2 area (Oliva et al., 2016). Beyond its intrinsic ability to generate SWRs, area CA3 has also been regarded as the site where new items of memory representations could be stored in the first place (Rolls and Kesner, 2006; Lisman, 1999). This suggests that the CA3 region possesses all of the requisites to guarantee the correct replay and consolidation of recent memory traces (Nakashiba et al., 2009). Recent findings, however, suggest that this process may be assisted by other brain areas. In support of this hypothesis, the SWR occurrence and spike content have been shown to be influenced by neocortical oscillations and by changes in cortical (Sirota et al., 2003; Battaglia et al., 2004; Isomura et al., 2006; Ji and Wilson, 2007; Sullivan et al., 2011; Wang and Ikemoto, 2016; Rothschild et al., 2017) and subcortical activity (Logothetis et al., 2012; Ramirez-Villegas et al., 2015). This suggests that brain regions beyond the CA3 network are important for SWR-dependent memory consolidation processes. In the present study, we demonstrate that besides the primary role of CA3 in SWR genesis, the subiculum can act as a secondary SWR generator. We also show that SWRs originated in the subiculum can travel forward to the cortex as well as backward to the hippocampus proper. This secondary source of SWRs may be complementary to CA3 to guarantee the correct consolidation of new memories.

RESULTS

Atypical origin of SWRs

We performed extracellular recordings using a 32-channel perforated multi-electrode array (pMEA) on acute horizontal slices containing CA3, CA2, CA1, dentate gyrus (DG), subiculum, and entorhinal cortex (EC). As previously reported, we observed spontaneously occurring SWRs (Papatheodoropoulos and Kostopoulos, 2002; Maier et al., 2003, 2009, 2011; Hájos et al., 2009; Donoso et al., 2018). Spontaneous SWRs were detected simultaneously in a large portion of recording channels in the CA1-subiculum area. The magnitude and polarity of the signals varied depending on the localization of the channels with respect to the hippocampal layers (Figures 1A and 1B). To our surprise, we observed that not all SWRs followed the classical propagation pathway from proximal to distal CA1 (Figure 1A, top). Instead, a portion of SWRs seemed to emerge at an atypical site (downstream to the CA3 area) and to propagate in the opposite direction (Figure 1A, bottom). The two different directions of propagation can be clearly observed in the pseudocolor maps presented in Figure 1D. The maps in Figure 1D (top) represents the standard propagation of the SWR event in Figure 1A (top) while the maps in Figure 1D (bottom) showed the propagation of the SWR event in Figure 1A (bottom) moving in the opposite direction. To quantify this phenomenon, we analyzed the direction of SWR propagation on a single-event basis. We defined two possible

directions: (1) a standard one, where SWRs appeared first in channels located in CA2 or proximal CA1 and moved toward more distal areas, and (2) an atypical one, where SWRs appeared in channels on the CA1 or subiculum and propagated either toward more proximal areas or bidirectionally. SWRs showing an atypical direction of propagation represented 13.1% of the total number of events (106 of 811, in 5 of 19 recordings from 6 mice) (Figure 1C). These data suggest that a portion of SWRs can apparently emerge downstream to CA3-CA2 and can back-propagate from distal to proximal locations along the CA axis.

Subiculum as a secondary SWR generator

Our pMEA recordings suggest that occasionally SWRs emerged at an atypical site. Therefore, we further investigated the existence and localization of a secondary SWR generator in the hippocampus, by performing simultaneous local field potential (LFP) recordings in the area CA3, CA1, and subiculum (Figure 2A). Consistent with previous studies, SWRs could be detected in all recorded regions (Maier et al., 2003, 2009; Wu et al., 2006; Eller et al., 2015); however, in comparison to CA3 and CA1, in the subiculum, the SWR appearance was more variable and ripple power was weaker (Table 1; Figure S2).

We analyzed the temporal relation between SWRs detected in the 3 different brain regions (see Method details) and observed both standard SWRs that emerged first in CA3 and SWRs that emerged first at locations downstream to CA3. This latter type likely corresponds to the SWRs, with atypical origin observed in the pMEA recordings, and will therefore be referred to as atypical SWRs in the following. Figure 2B shows the voltage traces of a standard event that appears first in CA3 and propagates toward CA1 and the subiculum. Figure 2D shows the voltage traces of an atypical SWR that appears first in the subiculum and moves "backward" to CA1 and CA3. To further emphasize the direction of SWR propagation, we plotted the wavelet spectrograms of the signals from the 3 different recording sites centered at the CA3-SWR peak. The increase in the ripple-band power in the standard SWR appeared first in CA3 and followed, with an increasing delay, in CA1 and the subiculum (Figure 3C). In contrast, in the example of atypical SWR, the increase in the ripple-band power emerged first in the subiculum and followed in CA1 and CA3 (Figure 2E).

SWRs are known to cause a strong increase in neuronal firing (Csicsvari et al., 2000). We therefore performed multi-unit activity (MUA) analysis from the three different recording sites (Figure 2F). The spike-time raster plots from one representative recording shows that neuronal firing in both CA1 and the subiculum can precede neuronal activity in CA3 (Figure 2G). Accordingly, the peri-SWR spike-time histogram (PSTH) presented a bimodal distribution in CA1 and subiculum (Figure 2H). The first peak at time <0 with respect to CA3-SWR peaks suggests that a consistent portion of SWRs in CA3 were preceded by neuronal activity in CA1 and the subiculum.

To assess the abundance of atypical SWRs, we determined the percentage of SWRs with respect to their putative region of origin (the region where they appeared first) in all of our recordings (23 recordings from 11 mice). As expected, the majority of SWRs emerged in CA3 first (82.5%, 6,541 of 7,929). SWRs with a putative origin in subiculum represented 14.7% of the total events (1,167 of 7,929), while the remaining 2.8% (221 of 7,929) had a putative origin in CA1 (Figure 2I). Finally, some SWRs were confined in their putative area of origin or propagate only partially (Figure 2J). We observed locally isolated SWRs in the area CA3 or in the CA3-CA1 region (2.9%, 233 of 7,929) as well as SWRs confined to the subiculum or to the CA1-subiculum region (6.9%, 543 of 7,929) (Figure 2K). We never observed SWRs confined to the CA1 area only. Importantly, SWRs with an atypical origin were more frequently observed in slices from the most ventral part of the hippocampus. We found a significant correlation between the percentage of SWRs with putative origin downstream to CA3 and the slice interaural distance (Figure S1A). Furthermore, the probability of SWRs to back-propagate from an atypical origin all the way to CA3 was also dependent on the slice location along the dorsoventral axis (the back-propagation to CA3 was observed only in the most ventral slices; see Figure S1B).

These findings provide evidence for a secondary SWR generator in the distal CA or in downstream regions. Based on our results, the subiculum is the brain area where this secondary SWR generator is most likely to reside; however, the presence of even a ternary generator cannot be ruled out.

Next, we compared different properties of the ripple component in standard and atypical SWRs. We found that standard CA3-SWRs had a higher number of ripple cycles and a stronger power in the ripple-frequency band compared to CA3-SWRs with atypical origin (Table 1; Figures S2A and S2B). We found similar differences with SWRs detected in the subiculum (Sub-SWRs). Atypically originated Sub-SWRs had a higher number of ripple cycles and a stronger power in the ripple band with respect to standard Sub-SWRs (Table 1; Figures S2C and S2D).

Recent studies reported that EC activity can precede hippocampal ripples (Sullivan et al., 2011, Yamamoto and Tonegawa, 2017). Based on these findings, it is plausible that a population burst or a ripple could emerge in the EC, travel toward the subiculum, and trigger what we refer to as atypically originated SWRs. To study the contribution of the EC in the emergence of atypical SWRs, we recorded from CA3, CA1, and subiculum before and after cutting out the EC from our slices (Figure 3A). Atypically originated SWRs could be observed, at similar probability, before and after the EC removal (before: 18.2%, 567 of 3,115; after: 16.5%, 596 of 3,619; 7 recordings from 5 mice, paired t test, $p > 0.05$) (Figures 3B and 3C). This shows that the EC is not necessary for the emergence of atypical SWRs in the subiculum.

To test whether the subiculum could generate SWRs on its own, we disconnected it from CA1 and from downstream parahippocampal structures (Figure 3D) (see STAR Methods). LFP recordings showed that the isolated subicular circuitry was capable of generating SWRs (Figure 3E), with an incidence of $0.08 \pm 0.02\ s^{-1}$ (6 slices from 3 mice). Simultaneous recordings in CA1 confirmed that SWRs detected in CA1 and subiculum were uncoupled (data not shown), corroborating the complete separation of the two structures by the cutting procedure.

Propagation of atypical SWRs into the EC

Next, we asked whether atypically originated SWRs could also travel to the EC. Since LFP signals from the EC are relatively

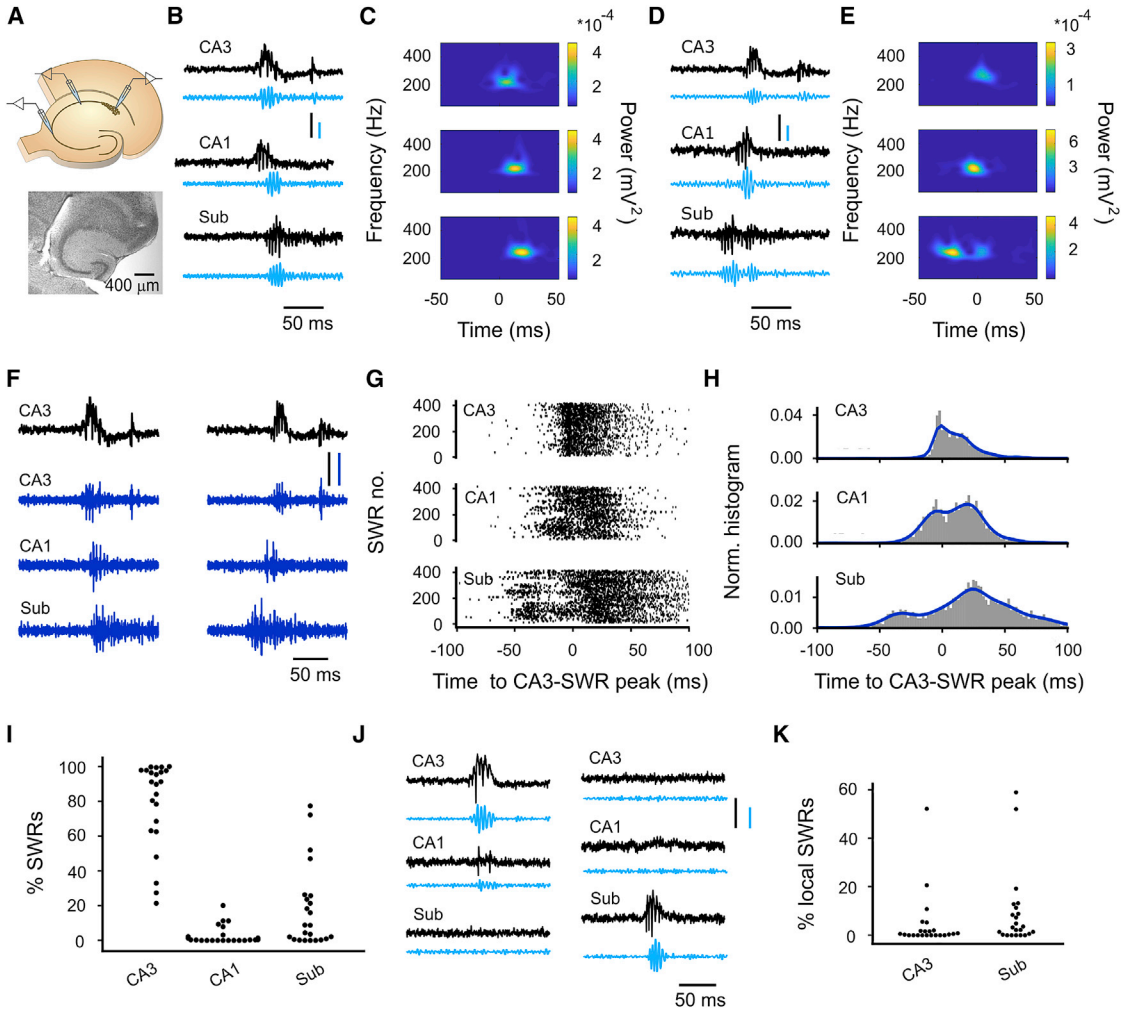

Figure 2. A secondary SWR generator in the subiculum

(A) The sites of simultaneous LFP recordings (top) and a representative Nissl staining of one of the probed slices (bottom).

(B and C) Representative raw (black) and ripple-filtered (150–300 Hz) (light blue) signals showing a SWR propagating along the standard path from CA3, to CA1 and subiculum (standard SWR) (B) and their respective ripple-filtered wavelet spectrograms (C). Time zero refers to the peak of the CA3-SWRs.

(D and E) Same as in (B) and (C), but for an event emerging first in the subiculum and propagating backward (atypical SWR). Scale bars in (B) and (D): 100 μV (black) and 40 μV (light blue).

(F) Representative raw (black) and multi-unit activity (MUA)-filtered (>500 Hz) (blue) signals from a standard (left) and an atypical SWR (right). Scale bars: 100 μV (black) and 100 μV (blue).

(G) Raster plots showing the timing of spikes in the 3 regions with respect to the peak of the CA3-SWRs in a representative recording.

(H) Normalized peri-SWR spike-time histogram and its kernel density estimate (blue lines) at the 3 different recording sites for the same recording shown in (G). Note the bimodal distribution particularly evident in the subiculum.

(I) Percentage of SWRs with respect to their region of origin.

(J) Example of a SWR locally confined to CA3-CA1 (left) or to the subiculum (right). Scale bars: 100 μV (black) and 50 μV (light blue).

(K) Percentage of locally confined SWRs with respect to their region of origin.

weak in slices, we combined CA3-LFP recordings with whole-cell recordings in the current-clamp configuration from excitatory neurons in the deep layers of the EC (Figure 4A). We checked whether, in our slice preparation, deep-layer EC neurons receive SWR-related inputs, as previously reported *in vivo* (Chrobak and Buzsáki, 1994) and *in vitro* (Roth et al., 2016). Confirming previous findings, we observed postsynaptic potentials (EC-PSPs) with a mean amplitude of 5.10 ± 0.63 mV time locked to SWRs in the majority of the recorded cells (40 of 51 from 28 mice) (Figure 4B).

When we aligned the EC-PSPs to the peak of the SWRs, we observed that in 60% of our recordings (24 of 40), a fraction of EC-PSPs did not follow CA3-SWRs but preceded them (Figure 4C). We assumed that the observed EC activity preceding CA3-SWRs was due to the propagation of atypically generated SWRs to the EC (Figures 1 and 2). Occasionally, we also

Table 1. Properties of SWRs depending on the recording site and on the putative region of interest (CA3 for standard and CA1 or subiculum for atypical SWRs)

	Recording site					
	CA3 (CA3-SWRs)			Subiculum (sub-SWRs)		
Ripple property	Standard	Atypical	p	Standard	Atypical	p
No. of cycles	6.10 ± 0.18	5.24 ± 0.43	0.05	5.35 ± 0.41	6.82 ± 0.41	0.03*
Power (mV^2)	0.090 ± 0.030	0.078 ± 0.027	0.03*	0.044 ± 0.005	0.061 ± 0.009	0.007*
Frequency (Hz)	214.1 ± 8.7	221 ± 6	0.45	244.8 ± 4.6	229.5 ± 9.5	0.07
Duration (ms)	34.70 ± 1.20	29.78 ± 2.58	0.07	32.31 ± 1.47	36.70 ± 1.55	0.07

p indicates the p values obtained with a paired Student's t test from 8 recordings from 5 mice. *, statistical significance.

observed that some CA3-SWRs did not generate any PSP in the recorded neuron. These events are likely to be SWRs confined to CA3 or CA3-CA1, as shown in Figures 2J and 2K. Considering all of the recordings in which EC activity before CA3-SWRs could be identified, SWRs followed by a EC-PSP (likely corresponding to standard SWRs) represented 68.5% (1,456 of 2,124) SWRs preceded by EC-PSP (likely corresponding to atypical SWRs) represented 16.6% (353 of 2,124), and SWRs that failed to propagate to the EC (local) represented 14.8% (315 of 2,124) of all events (Figure 4D). Further corroborating the presence of EC activity before hippocampal SWRs, the peri-CA3-SWR, EC-PSP peak-time histogram showed a bimodal distribution, with two clear peaks—one with a negative delay and one with a positive delay with respect to CA3-SWR peaks (Figure 4E).

Then, to confirm that the EC activity preceding hippocampal SWRs was due to the propagation of atypical SWRs originated in the subiculum, we combined LFP recordings from CA3 with simultaneous whole-cell recordings from excitatory neurons in the EC and in the subiculum. Here, we performed patch-clamp, voltage-clamp recordings to achieve a higher temporal resolution in comparing the timing of postsynaptic currents (PSCs) in the two recorded cells. SWRs were categorized as standard or atypical depending on the CA3-SWR to EC-PSC latency. Atypical SWRs were observed in 19.9% of all events (141 of 709, in 5 of 22 simultaneous recordings, 19 mice). For standard SWRs, both subicular- and EC-PSCs followed CA3-SWRs, in that order. Conversely, for atypical SWRs, both subicular- and EC-PSCs preceded CA3-SWRs (Figure 5A). Figure 5B illustrates the average of all subicular- and EC-PSCs, from one recording, separated according to their standard or atypical origin (black and gray traces, respectively), demonstrating that both subicular and EC neurons received synaptic inputs preceding CA3-SWRs. In line with this, the peri-CA3-SWR, PSC onset-time histogram showed a similar bimodal distribution in both EC and subicular recordings (Figure 5C). To verify that the activity preceding SWRs emerged first in the subiculum and then propagated to the EC, we analyzed the time course of such histograms. The two peaks in the subicular-PSC/CA3-SWRs histograms occurred ~8 ms before the peaks in the EC-PSC/CA3-SWRs histograms (subiculum peaks: −22.68 and 4.46 ms, EC peaks: −14.22 and 12.23 ms, respectively; Figure 5C). This suggests both the presence of a secondary SWR generator downstream to CA3, presumably in the subiculum, and synaptic activity in EC neurons following atypically originated SWRs.

Finally, we asked whether, after traveling to the EC, atypically originated SWRs could re-enter the hippocampus. Since the DG represents the first stage along the perforant pathway, we tested this possibility by performing CA3-LFP with simultaneous whole-cell recordings from EC and DG granule cells (Figure 5D). DG granule cells were recently reported to receive SWR-related inputs via a disynaptic pathway, involving a back-propagation from CA3 via mossy cells (Swaminathan et al., 2018). In line with this, we observed DG granule cell-PSCs (DG-PSCs) delayed with respect to the CA3-SWRs (Figure 5D). Based on the CA3-SWR to EC-PSC latency, we observed atypical SWRs in 4 of 8 recordings (from 6 mice); however, we never observed DG-PSCs before CA3-SWRs for both EC-PSCs that preceded or followed the CA3-SWRs (Figure 5D). We computed the average of the DG-PSCs and EC-PSCs for all of the PSCs associated with standard and atypical SWRs (Figure 5E). While EC-PSCs associated with standard SWRs (black traces) and atypical SWRs (gray traces) had a very different time course and only marginally overlapped (Figure 5E, bottom), DG-PSCs associated with standard and atypical SWRs had a similar time course and overlapped extensively (Figure 5E, center). Furthermore, EC-PSCs associated with atypical SWRs preceded CA3-SWRs (Figure 5E, top and bottom, gray traces), while DG-PSCs associated with atypical SWRs always followed the SWR occurrence (Figure 5E, top and center, gray traces). The unimodal distribution in the peri CA3-SWR, DG-PSC onset-time histogram with a peak at time > 0 (Figure 5F) further confirmed the lack of synaptic activity onto DG granule cells before CA3-SWRs.

Propagation of SWRs *in vivo*

Our *in vitro* data provide several lines of evidence for the presence of a secondary SWR generator in the subicular area. Furthermore, in a series of combined LFP and juxtacellular recordings in head-fixed mice, we noticed that the firing of subicular neurons whose activity was significantly modulated by CA1-SWRs often preceded the peak of SWRs detected in CA1 (Figure S3). This was surprising, since the peak of increase in neuronal firing in a hippocampal region generally coincides with the ripple-peak detected in the same region (Oliva et al., 2016). This observation, together with our *in vitro* findings, encouraged us to further investigate the potential role of the subiculum as a secondary SWR generator in the intact brain. To this end, we performed multisite recordings from CA1 and the

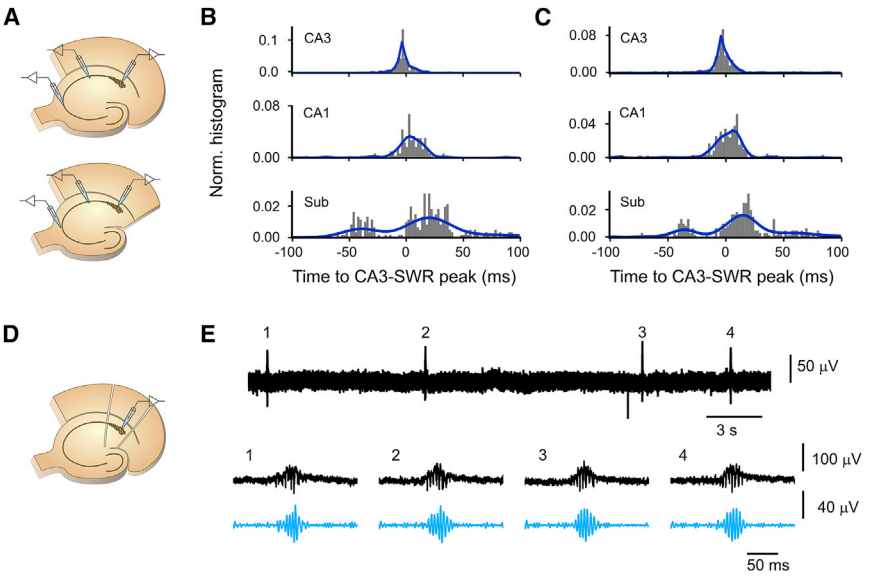

Figure 3. The subiculum as independent, secondary SWR generator

(A) The recording sites of a hippocampal slice before (top) and after (bottom) removal of the entorhinal cortex (EC).

(B and C) Normalized peri-SWR spike-time histograms and their kernel density estimates (blue lines) at the 3 different recording sites before (B) and after (C) the removal of the EC in the same slice.

(D) The recording in the isolated subiculum.

(E) Representative LFP recording from the subiculum (top). The detected SWRs are marked with the numbers 1–4. On the bottom, the detected SWRs (raw and ripple filtered signals, in black and blue, respectively) are displayed at higher temporal resolution.

subiculum in freely behaving rats and analyzed the ripple propagation across these areas as well as the concomitant neuronal firing. We chose to perform the experiments in rats because of the larger brain dimensions, facilitating the insertion of two probes in the neighboring CA1 and subiculum (Figure 6A), and given the high similarity in structure and connectivity with the mouse brain.

Previous *in vivo* work showed that SWRs travel unidirectionally from CA3-CA2 to downstream areas. However, SWRs propagation has always been studied by averaging all SWRs detected in a given recording session (Csicsvari et al., 2000; Oliva et al., 2016). This approach is justifiable, because it increases the signal-to-noise ratio and therefore permits measuring very short time delays between LFP signals from neighboring regions. However, a drawback of this method is that it can mask atypical propagations if these represent a minority of events. In the attempt to overcome this limitation, we analyzed the ripple propagation on a single-event basis.

In accordance with previous simultaneous recordings from CA1 and EC (Chrobak and Buzsáki, 1996), we found that the majority of the ripples displayed either a clear propagation delay from CA1 to the subiculum (56.5%, 577 of 1,031 events; average time lag of CA1 → subiculum peak power: 6.51 ± 1.96 ms) or occurred virtually simultaneously in the 2 brain structures (30.5%, 314 of 1,031 events; average time lag of CA1 → subiculum peak power: −1.03 ± 1.18 ms) (from 3 rats). However, in the remaining 13.6% (140 of 1,031), we observed an inverse propagation (average time lag CA1 → subiculum peak power time: −3.43 ± 2.14 ms). Figure 6B shows a ripple episode with standard propagation and another ripple episode propagating in atypical fashion from the same recording. Each trace represents the normalized ripple-centered raw signal moving, from top to bottom, from proximal to distal CA1 (blue) and from proximal to distal subiculum (red) (one signal per shank). Furthermore, for better visualization of the timing of standard and atypical ripples along the CA1-subiculum axis, we present the ripple-triggered wavelet spectrograms corresponding to the four most proximal shanks from CA1 and subiculum in Figure 6C.

Next, we analyzed the firing of CA1 and subicular units separately for ripples classified as standard and atypical. The spike time distributions and corresponding raster plots, both centered to the subicular ripple maximum, show that CA1 firing is leading subicular firing during standard ripples (Figures 6D and 6E, left), while CA1 followed subicular units during atypical ripples (Figures 6D and 6E, right). We quantified the time differences for STHs of CA1 neurons representing standard and atypical ripples. Specifically, we measured the time at which each ripple positively modulated CA1 neuron (standard n = 89, atypical n = 81) reached 50% of its spikes considering all spikes detected in a window of ±250 ms from the ripple peak. The 50th percentile of CA1 cells spikes occurred at significantly earlier time points during standard ripples with respect to their atypical counterparts (Figure 6F) (Mann-Whitney *U* test, p = 0.0012).

Our findings demonstrate that ripples and ripple-associated firing in the subiculum can precede ripples occurring in CA1, thereby establishing the presence of atypically originated ripples in the intact brain.

DISCUSSION

SWRs are believed to play a central role in memory consolidation by promoting the replay of memory traces acquired during recent behavior and by promoting their transfer from the hippocampus to the cortex for long-term storage (Girardeau and Zugaro, 2011). Despite the undisputed, central role of CA3 in the initiation of SWRs, a growing number of studies reported that cortical up and down states and episodes of increased cortical activity can bias the occurrence and the content of SWRs (Sirota et al., 2003; Battaglia et al., 2004; Isomura et al., 2006; Sullivan et al., 2011; Wang and Ikemoto, 2016; Rothschild et al., 2017). This suggests that, under some circumstances, CA3 may require external instructive inputs to initiate SWRs at the right time and/or to select the right neuronal ensembles. The present results complement this theoretical framework, providing

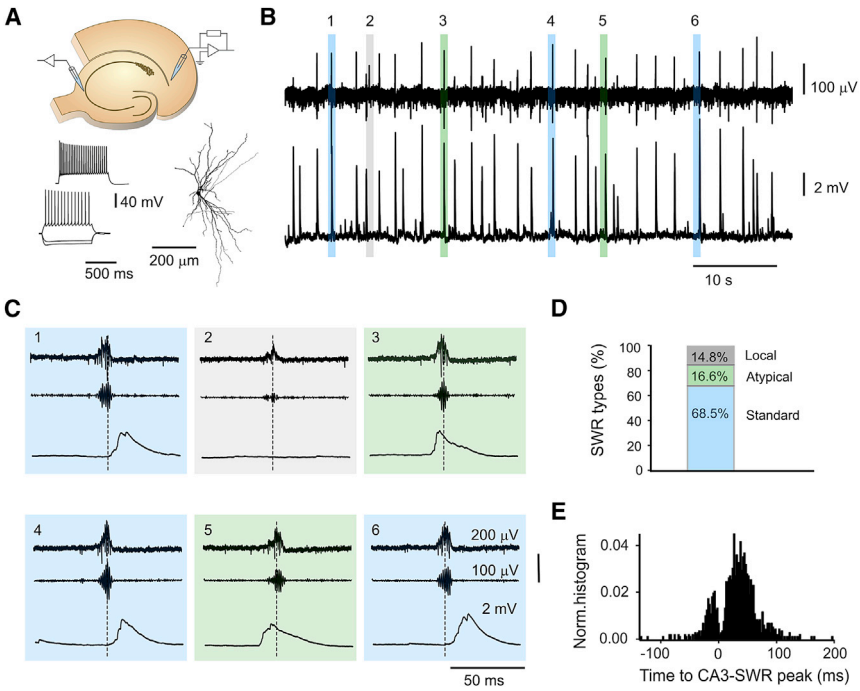

Figure 4. Propagation of standard and atypical SWRs in the EC

(A) The location of the LFP and patch-clamp recordings (top) and the reconstruction of a neuron recorded in the deep layers of the EC (bottom right) with the respective voltage traces in response to step currents (−280, −160, 200, and 400 pA) (bottom left).

(B) LFP recording from the area CA3 showing spontaneously occurring SWRs (top) and simultaneous whole-cell current-clamp recording from an EC deep layer neuron (bottom). The presence of postsynaptic potentials (EC-PSPs) coupled to SWRs demonstrates the efficient propagation of SWRs in hippocampal-entorhinal slices.

(C) The SWR-PSP pairs in the colored shaded boxes in (B) are displayed at a higher temporal resolution. Note the presence of CA3-SWRs followed (blue) and preceded (green) by an EC-PSP, most likely corresponding to standard and atypically originated SWRs, and an event that failed to propagate to the EC (gray).

(D) Percentage of standard, atypical, and locally confined SWRs in all recordings in which both standard and atypical SWRs were detected.

(E) Normalized peri-SWR EC-PSP-time histogram from all recordings in which both standard and atypical SWRs were detected. Note the bimodal distribution of the histogram emphasizing the presence of 2 different temporal associations between CA3-SWRs and synaptic inputs in the EC.

evidence that the subiculum also plays a substantial role in SWR generation.

A portion of SWRs have an atypical origin

To study the propagation of SWRs in the hippocampus, we took advantage of an *in vitro* model of SWRs (Maier et al., 2003). By combining multi-electrode array-clamp (Figure 1), multiple LFP-clamp (Figures 2 and 3), and patch-clamp recordings (Figures 4 and 5) from different hippocampal and para-hippocampal areas, we demonstrate that a small but consistent portion of SWRs have an atypical origin downstream to the CA3-CA2 subfield. Most frequently, atypically originated SWRs appeared in the subiculum at first and traveled backward toward upstream hippocampal regions, suggesting that the main output structure of the hippocampus may function as a secondary SWR generator. In line with our findings, an *in vitro* study using calcium imaging reported that a portion of subicular neurons were active before CA1-SWRs (Norimoto et al., 2013); furthermore, for subicular burst firing neurons, Böhm et al. (2015) reported a bimodal spike-time distribution associated with SWRs, in which 1 peak was 40 ms before and a second coincided with the CA1-ripple maximum. This unexpected early activation of subicular neurons is consistent with the atypically generated SWRs described in the present study.

Interestingly, we found that the ripple component of SWRs was stronger, in terms of power and number of oscillation cycles, in the putative region of origin and weaker after propagation into other hippocampal areas (Table 1; Figure S2). The power of extracellular ripple oscillations has been linked to the summation of postsynaptic inhibitory currents in spatially arranged pyramidal neurons (Ylinen et al., 1995, Schlingloff et al., 2014; Donoso et al., 2018) and to the coherence of principal neuronal firing (Csicsvari et al., 2000; Schomburg et al., 2012). Based on these lines of evidence, the weakening ripple component may suggest a progressively less efficient spatiotemporal recruitment of neurons along their journey. It is plausible to assume that a strong ripple component may be important for a precise replay of spike sequences representing recent experiences. A secondary SWR generator in the subiculum may therefore be important to guarantee a correct replay of specific spike sequences along all stations from the hippocampus to the cortex. Beyond the subiculum, we cannot exclude the area CA1 and other parahippocampal areas as possible secondary SWR generators. Future studies using large-scale high-density recordings or neuronal population imaging, covering hippocampal and retrohippocampal areas, will be necessary to precisely locate the site of origin of atypically generated SWRs or to disclose whether multiple sites of origin exist.

Another interesting observation was that the percentage of atypical SWRs was higher in slices from the most ventral part of the hippocampus. Furthermore, the extent to which atypical SWRs back-propagated to CA3 was also influenced by the location of the slices along the dorsoventral axis (Figure S1). These results may suggest that either a different connectivity scheme, a larger degree of recurrent connectivity, and/or different physiological properties in the most ventral subiculum favor the emergence of SWRs. However, another hypothesis to explain these findings could be that during the slice preparation procedure, fibers may be severed to a different degree, depending on the dorsoventral level. Supporting this idea, the appearance of the

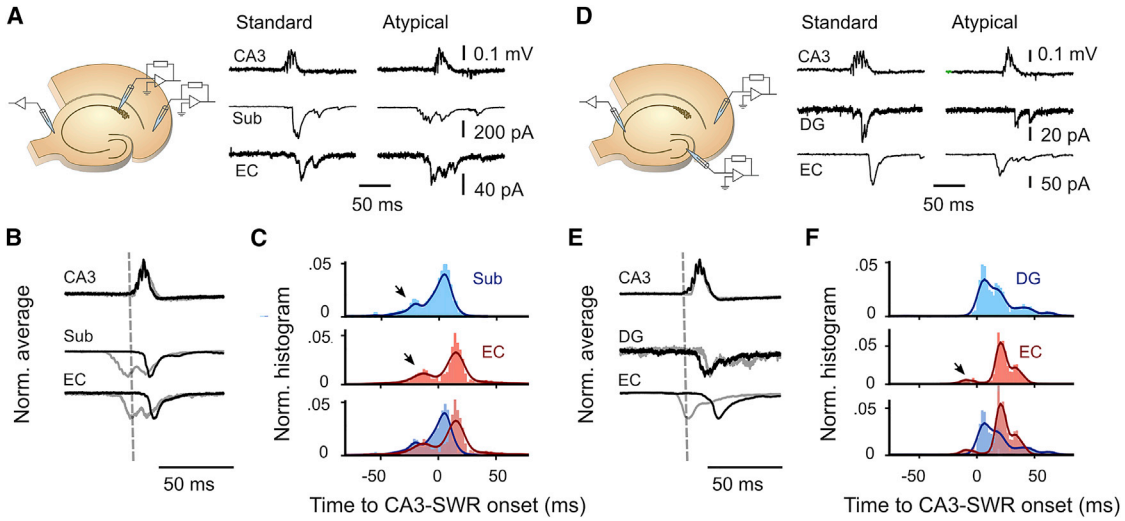

Figure 5. SWRs with atypical origin propagate to the EC, but do not re-enter the hippocampus via dentate gyrus (DG)

(A) Illustration (left) and representative traces (right) of simultaneous CA3-LFP and dual whole-cell recordings from neurons in the subiculum (Sub) and in the deep layers of the EC (EC).

(B) Average of voltage signals from all standard and atypical SWRs (black and gray, respectively) (top) and for the associated PSCs in a subicular (center) and an EC neuron (bottom) in 1 recording.

(C) Normalized peri-SWR PSC onset-time histogram and its kernel density estimate (solid lines) from all double-patch clamp recordings with subicular (blue) and EC (red) neurons in which both standard and atypical SWRs were detected (overlaid histograms, bottom). Note similar bimodal distributions in both histograms.

(D) Illustration (left) and representative traces (right) of simultaneous CA3-LFP and dual whole-cell recordings from a DG granule cell (DG) and a neuron in the deep layers of the EC (EC). Note the absence of DG granule cells inputs before the CA3-SWR.

(E) Average voltage signals from all standard (black) and atypical (gray) SWRs (top) and for the associated PSCs in a DG granule cell (center) and an EC neuron (bottom) in 1 recording.

(F) Normalized peri-SWR PSC onset-time histogram and its kernel density estimate (solid lines) from all DG (blue) and EC neuron recordings (red), in which both standard and atypical SWRs were detected (overlaid histograms, bottom). Note the absence of bimodality for DG data.

hippocampus in horizontal slices changes drastically moving from ventral to more dorsal locations (Franklin and Paxinos, 2007). Therefore, it is possible that the lack (or very low percentage) of atypical SWRs at more dorsal locations *in vitro* may be due to a less optimal preservation of the neuronal circuitry in less ventral slices. Supporting this hypothesis, our *in vivo* recordings (Figure 6) showed that ripples originating downstream of CA1 are likely to occur in the dorsal hippocampus. Furthermore, as a potential structural property that underlies the backpropagation of SWRs, subicular neurons back-projecting to CA1 were found in the dorsal hippocampus (Sun et al., 2014, 2018). Therefore, even though we cannot exclude that differences in hippocampal circuitry along the dorsoventral axis may account for the observed correlations (Figure S1), the above-mentioned lines of evidence suggest that the capacity to generate atypical SWRs may not be an exclusive property of the ventral subiculum.

Subiculum as secondary SWR generator

Recent studies reported a bidirectional communication between cortex and hippocampus during SWRs (Sullivan et al., 2011; Wang and Ikemoto, 2016; Rothschild et al., 2017). Furthermore, ripples originated in the EC have been shown to occur before CA1-SWRs (Yamamoto and Tonegawa, 2017). This suggests that EC activity may enter the hippocampus via the temporoammonic path and trigger SWRs directly in CA1 or the subiculum. Even if we cannot rule out a contribution of the EC in the emergence of the atypically originated SWRs we reported here, our multiple LFP recordings performed before and after the removal of the EC from our slices (Figures 3A–3C) demonstrated that the inputs from this cortical area are not necessary for the generation of atypical SWRs. In light of this finding, it is plausible to assume that the subiculum may act as a secondary site of SWR origin independent of inputs from other brain areas.

Based on a number of observations, the subiculum is likely to be equipped with all of the elements needed for the emergence of SWRs. First, we observed spontaneous SWRs in the subiculum even when it was separated from up- and downstream brain regions (Figures 3D and 3E). Second, the subiculum has been shown to be capable of a self-generating synchronous population burst (Harris and Stewart, 2001) and to have a high recurrent connectivity among excitatory neurons (Böhm et al., 2015). Remarkably, the connectivity rate between subicular regular and burst firing neurons and from regular to burst firing neurons was found to be 3–8 times higher than the connectivity between pyramidal neurons in CA3 (Böhm et al., 2015; Guzman et al., 2016). Furthermore, a previous study by our group showed that optogenetic stimulation of subicular bursting neurons can reliably induce ripple-band oscillations (Nitzan et al., 2020), providing additional causal evidence for the subiculum to work as a SWR generator.

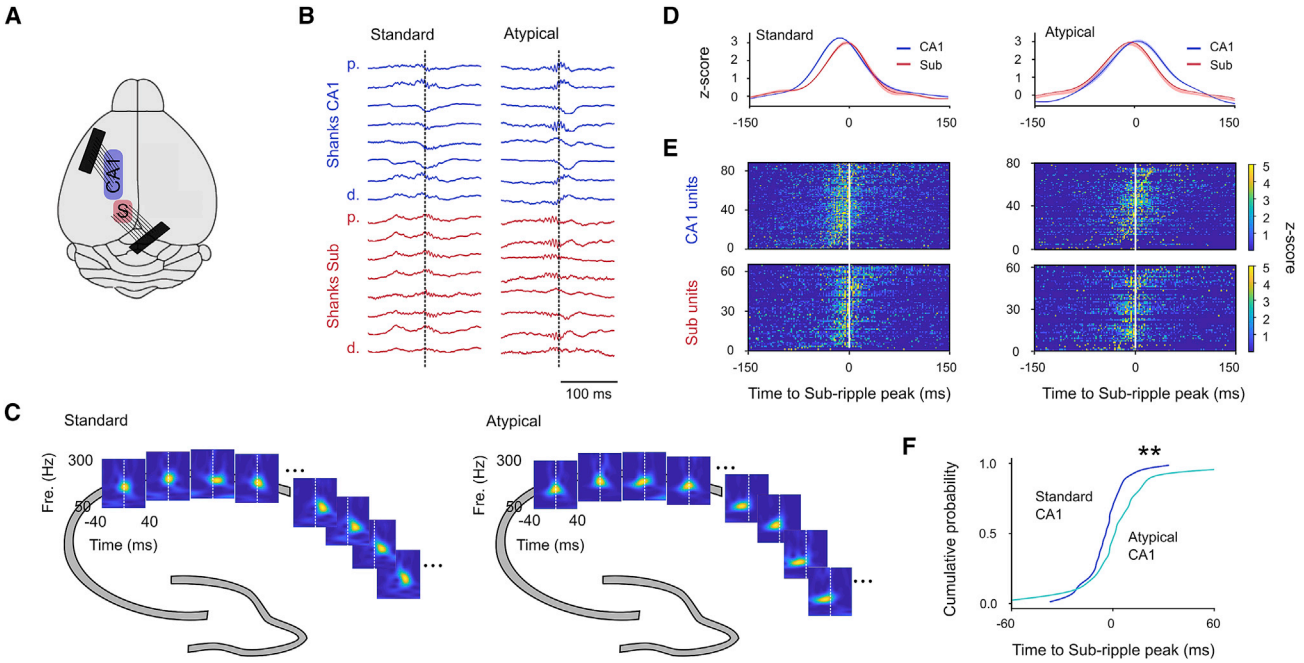

Figure 6. Standard and atypical ripple propagation in freely moving rats *in vivo*

(A) Representative illustration showing the position of the 2 probes in CA1 and the subiculum.

(B) Representative LFP traces showing a ripple epoch with standard propagation from CA1 to subiculum (left) and atypical propagation from subiculum to CA1 (right). Each trace represents the ripple-centered signal from the channel displaying the highest power in the ripple band for each shank (from top to bottom: proximal (p.)–distal (d.) CA1, blue; subiculum, red. For better visualization of the timing of the signals, amplitudes are displayed in arbitrary values.

(C) Normalized ripple-triggered wavelet spectrograms; the 4 most proximal CA1 and subiculum channels in (B) are shown. Note the difference in timing for standard and atypical ripples.

(D and E) Peri-ripple *Z* scored means (lines) ± SEMs (lighter areas) spike time (D) histograms and (E) raster plots from all units detected in CA1 and subiculum showing that the recruitment of neurons in both areas follows a different temporal order for standard (left) or atypical (right) ripples.

(F) Cumulative probability functions for CA1 units during standard and atypical ripples (89 and 81 neurons, respectively, from 4 recordings from 2 rats) representing time points at which CA1 units reach 50% of their total spike counts in a window of ±250 ms from the peak of subicular ripples. Ripple-related firing occurs later in atypical compared to standard ripples (Mann-Whitney *U* test, p = 0.0012).

Propagation pathways of atypical SWRs

Our simultaneous whole-cell patch clamp and CA3-LFP recordings showed that atypically originated SWRs, as their standard counterparts, traveled into the subiculum and recruited EC neurons (Figures 4 and 5A–5C). Nonetheless, atypically originated SWRs could also propagate backward from the subiculum to CA1 and CA3 (Figure 2). We can exclude that this observation is due to the re-entrance of SWRs from the EC to the CA3 area via the DG since the back-propagation to CA3 was observed even after removal of the EC (Figures 3A–3C). Furthermore, our simultaneous patch-clamp recordings showed that synaptic inputs in DG granule cells never preceded CA3-SWRs, even when this happened in the simultaneously recorded EC neurons (Figures 5D–5F), which is in line with recent reports (Swaminathan et al., 2018).

The back-propagation to CA1 could be explained on the background of recent anatomical studies revealing the existence of non-canonical connections from the subiculum to CA1 (Sun et al., 2014, 2018; Xu et al., 2016). Furthermore, a very recent study reported excitatory projections from the subicular complex to CA3 (Lin et al., 2021).

An alternative hypothesis could rely on the propagation of activity depending on inhibitory back-projections reported both at the anatomical (Sik et al., 1994; Szabo et al., 2017) and the functional levels (Szabo et al., 2017). Furthermore, a previous study showed an inhibition-dependent reverse flow of information from the subiculum to CA1 and CA3 during theta oscillations (Jackson et al., 2014). Based on these findings, back-propagating SWRs may recruit back-projecting inhibitory neurons, which may temporarily suppress and then synchronize neuronal firing, thereby promoting, with a short delay, the emergence of SWRs (Ellender et al., 2010).

Atypical ripples *in vivo*

Finally, our simultaneous CA1 and subiculum recordings from freely behaving rats gave us the opportunity to explore whether the atypical SWRs observed *in vitro* could also be found in the intact brain. Our careful ripple-by-ripple examination revealed that the propagation delay of ripples between CA1 and the subiculum can substantially vary. Importantly, we could observe a consistent portion of ripples moving from the subiculum to CA1 (Figures 6B and 6C). During these atypical ripples, subicular neurons were also found to be recruited before CA1 neurons

(Figures 6D and 6E). These findings support the presence of a secondary SWR generator in the subiculum of awake rodents. Even if we cannot exclude that the observed variability in ripple propagation could emerge from standard CA3 ripples originated far from our recording site along the septo-temporal axis (Patel et al., 2013) or from ripples originated in the EC (Yamamoto and Tonegawa, 2017), our *in vivo* findings strongly suggest reconsidering the dogma that hippocampal SWRs originate exclusively from CA3-CA2. Finally, these *in vivo* results, obtained from the dorsal hippocampus, further suggest that atypical SWRs may not be a unique signature of the ventral hippocampus, but that they may be found along the whole dorsoventral axis.

Possible function of SWRs with atypical origin

The location of the secondary SWR generator, found in the present study, corresponds to the target of the temporoammonic projections, namely CA1 and the subiculum. These hippocampal areas represent the site where filtered and processed inputs from the trisynaptic pathway meet and become integrated with the direct inputs from the temporoammonic pathway (Vinogradova, 2001; Ang et al., 2005). The emergence of SWRs at this site may be important for the replay of memory traces complementary to those stored in CA3. Furthermore, due to the extensive reciprocal connections between the subiculum and thedifferent subcortical structures (O'Mara, 2005), one could speculate that SWRs generated at this site may play a role in integrating activity patterns of cognitive neuronal networks with those related to the autonomic nervous system. Finally, the existence of back-traveling SWRs may be important to provide instructing feedback inputs to the hippocampus proper. Many computational studies suggest that back-propagating functional connections are required for the hippocampus to function as an associative network with self-learning capacity (for a review, see Buzsáki, 2015).

STAR★METHODS

Detailed methods are provided in the online version of this paper and include the following:

- KEY RESOURCES TABLE
- RESOURCE AVAILABILITY
  - Lead contact
  - Materials availability
  - Data and code availability
- EXPERIMENTAL MODEL AND SUBJECT DETAILS
  - Mice
  - Rats
- METHOD DETAILS
  - Slice preparation
  - *In vitro* electrophysiology
  - Multi-electrode array recordings
  - Field and patch clamp recordings
  - *In vivo* juxtacellular recordings
  - *In vivo* silicon probes recordings
- QUANTIFICATION AND STATISTICAL ANALYSIS
  - Data analysis
  - Analysis on *in vitro* MEA recordings
  - Analysis on *in vitro* field recordings
  - Analysis on *in vitro* patch clamp recordings
  - Analysis on *in vivo* recordings
  - Statistics

SUPPLEMENTAL INFORMATION

Supplemental information can be found online at https://doi.org/10.1016/j.celrep.2021.109021.

ACKNOWLEDGMENTS

We thank S. Rieckmann, A. Schönherr, and J. Neugebauer for technical assistance and Prof. J.R.P. Geiger for giving us the opportunity to work on the pMEA system in his laboratory. We thank SciDraw (Jason Keller) for the mouse brain schematic in Figure 6. This work was supported by the German Research Council (Deutsche Forschungsgemeinschaft [DFG], projects 12959370-SFB 665, 184695641-SFB 958, 42860621-FOR 926, and 220176618-SPP1665), Germany's Excellence Strategy (EXC-2049-390688087 and EXC-2151-390873048), and the National Institute of Mental Health (NIMH), project R00 MH118423.

AUTHOR CONTRIBUTIONS

Conceptualization, B.I., N.M., and D.S.; formal analysis, B.I., N.N., and J.R.D.; methodology, N.M.; investigation, B.I., S.M., A.S., C.B., and N.M.; data curation, B.I.; writing – review & editing, B.I., N.N., J.R.D., and D.S.; visualization, B.I.; supervision, D.S.; funding acquisition, D.S.

DECLARATION OF INTERESTS

The authors declare no competing interests.

Received: October 27, 2020
Revised: February 22, 2021
Accepted: March 31, 2021
Published: April 20, 2021

REFERENCES

Ang, C.W., Carlson, G.C., and Coulter, D.A. (2005). Hippocampal CA1 circuitry dynamically gates direct cortical inputs preferentially at theta frequencies. J. Neurosci. *25*, 9567–9580.

Battaglia, F.P., Sutherland, G.R., and McNaughton, B.L. (2004). Hippocampal sharp wave bursts coincide with neocortical "up-state" transitions. Learn. Mem. *11*, 697–704.

Böhm, C., Peng, Y., Maier, N., Winterer, J., Poulet, J.F., Geiger, J.R., and Schmitz, D. (2015). Functional diversity of subicular principal cells during hippocampal ripples. J. Neurosci. *35*, 13608–13618.

Bragin, A., Jandó, G., Nádasdy, Z., van Landeghem, M., and Buzsáki, G. (1995). Dentate EEG spikes and associated interneuronal population bursts in the hippocampal hilar region of the rat. J. Neurophysiol. *73*, 1691–1705.

Buzsáki, G. (1986). Hippocampal sharp waves: their origin and significance. Brain Res. *398*, 242–252.

Buzsáki, G. (1989). Two-stage model of memory trace formation: a role for "noisy" brain states. Neuroscience *31*, 551–570.

Buzsáki, G. (1998). Memory consolidation during sleep: a neurophysiological perspective. J. Sleep Res. *7* (*Suppl 1*), 17–23.

Buzsáki, G. (2015). Hippocampal sharp wave-ripple: a cognitive biomarker for episodic memory and planning. Hippocampus *25*, 1073–1188.

Chrobak, J.J., and Buzsáki, G. (1994). Selective activation of deep layer (V-VI) retrohippocampal cortical neurons during hippocampal sharp waves in the behaving rat. J. Neurosci. *14*, 6160–6170.

Chrobak, J.J., and Buzsáki, G. (1996). High-frequency oscillations in the output networks of the hippocampal-entorhinal axis of the freely behaving rat. J. Neurosci. *16*, 3056–3066.

Csicsvari, J., and Dupret, D. (2013). Sharp wave/ripple network oscillations and learning-associated hippocampal maps. Philos. Trans. R. Soc. Lond. B Biol. Sci. *369*, 20120528.

Csicsvari, J., Hirase, H., Mamiya, A., and Buzsáki, G. (2000). Ensemble patterns of hippocampal CA3-CA1 neurons during sharp wave-associated population events. Neuron *28*, 585–594.

Donoso, J.R., Schmitz, D., Maier, N., and Kempter, R. (2018). Hippocampal ripple oscillations and inhibition-first network models: frequency dynamics and response to GABA modulators. J. Neurosci. *38*, 3124–3146.

Ego-Stengel, V., and Wilson, M.A. (2010). Disruption of ripple-associated hippocampal activity during rest impairs spatial learning in the rat. Hippocampus *20*, 1–10.

Ellender, T.J., Nissen, W., Colgin, L.L., Mann, E.O., and Paulsen, O. (2010). Priming of hippocampal population bursts by individual perisomatic-targeting interneurons. J. Neurosci. *30*, 5979–5991.

Eller, J., Zarnadze, S., Bäuerle, P., Dugladze, T., and Gloveli, T. (2015). Cell type-specific separation of subicular principal neurons during network activities. PLoS ONE *10*, e0123636.

Fernández-Ruiz, A., Oliva, A., Fermino de Oliveira, E., Rocha-Almeida, F., Tingley, D., and Buzsáki, G. (2019). Long-duration hippocampal sharp wave ripples improve memory. Science *364*, 1082–1086.

Franklin, K.B.J., and Paxinos, G. (2007). The Mouse Brain in Stereotaxic Coordinates, Third Edition (Elsevier).

Girardeau, G., and Zugaro, M. (2011). Hippocampal ripples and memory consolidation. Curr. Opin. Neurobiol. *21*, 452–459.

Girardeau, G., Benchenane, K., Wiener, S.I., Buzsáki, G., and Zugaro, M.B. (2009). Selective suppression of hippocampal ripples impairs spatial memory. Nat. Neurosci. *12*, 1222–1223.

Guzman, S.J., Schlögl, A., Frotscher, M., and Jonas, P. (2016). Synaptic mechanisms of pattern completion in the hippocampal CA3 network. Science *353*, 1117–1123.

Hájos, N., Ellender, T.J., Zemankovics, R., Mann, E.O., Exley, R., Cragg, S.J., Freund, T.F., and Paulsen, O. (2009). Maintaining network activity in submerged hippocampal slices: importance of oxygen supply. Eur. J. Neurosci. *29*, 319–327.

Harris, E., and Stewart, M. (2001). Intrinsic connectivity of the rat subiculum: II. Properties of synchronous spontaneous activity and a demonstration of multiple generator regions. J. Comp. Neurol. *435*, 506–518.

Hazan, L., Zugaro, M., and Buzsáki, G. (2006). Klusters, NeuroScope, NDManager: a free software suite for neurophysiological data processing and visualization. J. Neurosci. Methods *155*, 207–216.

Isomura, Y., Sirota, A., Ozen, S., Montgomery, S., Mizuseki, K., Henze, D.A., and Buzsáki, G. (2006). Integration and segregation of activity in entorhinal-hippocampal subregions by neocortical slow oscillations. Neuron *52*, 871–882.

Jackson, J., Amilhon, B., Goutagny, R., Bott, J.B., Manseau, F., Kortleven, C., Bressler, S.L., and Williams, S. (2014). Reversal of theta rhythm flow through intact hippocampal circuits. Nat. Neurosci. *17*, 1362–1370.

Ji, D., and Wilson, M.A. (2007). Coordinated memory replay in the visual cortex and hippocampus during sleep. Nat. Neurosci. *10*, 100–107.

Khodagholy, D., Gelinas, J.N., and Buzsáki, G. (2017). Learning-enhanced coupling between ripple oscillations in association cortices and hippocampus. Science *358*, 369–372.

Kudrimoti, H.S., Barnes, C.A., and McNaughton, B.L. (1999). Reactivation of hippocampal cell assemblies: effects of behavioral state, experience, and EEG dynamics. J. Neurosci. *19*, 4090–4101.

Lee, A.K., and Wilson, M.A. (2002). Memory of sequential experience in the hippocampus during slow wave sleep. Neuron *36*, 1183–1194.

Lin, X., Amalraj, M., Blanton, C., Avila, B., Holmes, T.C., Nitz, D.A., and Xu, X. (2021). Non-canonical projections from ventral CA1 and subicular complex to CA3 augments the feedforward hippocampal trisynaptic pathway. bioRxiv. https://doi.org/10.1101/2021.02.01.429124.

Lisman, J.E. (1999). Relating hippocampal circuitry to function: recall of memory sequences by reciprocal dentate-CA3 interactions. Neuron *22*, 233–242.

Logothetis, N.K., Eschenko, O., Murayama, Y., Augath, M., Steudel, T., Evrard, H.C., Besserve, M., and Oeltermann, A. (2012). Hippocampal-cortical interaction during periods of subcortical silence. Nature *491*, 547–553.

Maier, N., Nimmrich, V., and Draguhn, A. (2003). Cellular and network mechanisms underlying spontaneous sharp wave-ripple complexes in mouse hippocampal slices. J. Physiol. *550*, 873–887.

Maier, N., Morris, G., Johenning, F.W., and Schmitz, D. (2009). An approach for reliably investigating hippocampal sharp wave-ripples in vitro. PLoS ONE *4*, e6925.

Maier, N., Tejero-Cantero, A., Dorrn, A.L., Winterer, J., Beed, P.S., Morris, G., Kempter, R., Poulet, J.F., Leibold, C., and Schmitz, D. (2011). Coherent phasic excitation during hippocampal ripples. Neuron *72*, 137–152.

Nádasdy, Z., Hirase, H., Czurkó, A., Csicsvari, J., and Buzsáki, G. (1999). Replay and time compression of recurring spike sequences in the hippocampus. J. Neurosci. *19*, 9497–9507.

Nakashiba, T., Buhl, D.L., McHugh, T.J., and Tonegawa, S. (2009). Hippocampal CA3 output is crucial for ripple-associated reactivation and consolidation of memory. Neuron *62*, 781–787.

Nitzan, N., McKenzie, S., Beed, P., English, D.F., Oldani, S., Tukker, J.J., Buzsáki, G., and Schmitz, D. (2020). Propagation of hippocampal ripples to the neocortex by way of a subiculum-retrosplenial pathway. Nat. Commun. *11*, 1947.

Norimoto, H., Matsumoto, N., Miyawaki, T., Matsuki, N., and Ikegaya, Y. (2013). Subicular activation preceding hippocampal ripples in vitro. Sci. Rep. *3*, 2696.

O'Mara, S. (2005). The subiculum: what it does, what it might do, and what neuroanatomy has yet to tell us. J. Anat. *207*, 271–282.

Oliva, A., Fernández-Ruiz, A., Buzsáki, G., and Berényi, A. (2016). Role of hippocampal CA2 region in triggering sharp-wave ripples. Neuron *91*, 1342–1355.

Pachitariu, M., Steinmetz, N., Kadir, S., Carandini, M., and Harris, K.D. (2016). Kilosort: realtime spike-sorting for extracellular electrophysiology with hundreds of channels. bioRxiv. https://doi.org/10.1101/061481.

Papatheodoropoulos, C., and Kostopoulos, G. (2002). Spontaneous, low frequency (approximately 2-3 Hz) field activity generated in rat ventral hippocampal slices perfused with normal medium. Brain Res. Bull. *57*, 187–193.

Patel, J., Schomburg, E.W., Berényi, A., Fujisawa, S., and Buzsáki, G. (2013). Local generation and propagation of ripples along the septotemporal axis of the hippocampus. J. Neurosci. *33*, 17029–17041.

Ramirez-Villegas, J.F., Logothetis, N.K., and Besserve, M. (2015). Diversity of sharp-wave-ripple LFP signatures reveals differentiated brain-wide dynamical events. Proc. Natl. Acad. Sci. USA *112*, E6379–E6387.

Rolls, E.T., and Kesner, R.P. (2006). A computational theory of hippocampal function, and empirical tests of the theory. Prog. Neurobiol. *79*, 1–48.

Roth, F.C., Beyer, K.M., Both, M., Draguhn, A., and Egorov, A.V. (2016). Downstream effects of hippocampal sharp wave ripple oscillations on medial entorhinal cortex layer V neurons in vitro. Hippocampus *26*, 1493–1508.

Rothschild, G., Eban, E., and Frank, L.M. (2017). A cortical-hippocampal-cortical loop of information processing during memory consolidation. Nat. Neurosci. *20*, 251–259.

Schlingloff, D., Káli, S., Freund, T.F., Hájos, N., and Gulyás, A.I. (2014). Mechanisms of sharp wave initiation and ripple generation. J. Neurosci. *34*, 11385–11398.

Schneider, C.A., Rasband, W.S., and Eliceiri, K.W. (2012). NIH Image to ImageJ: 25 years of image analysis. Nat. Methods *9*, 671–675.

Schomburg, E.W., Anastassiou, C.A., Buzsáki, G., and Koch, C. (2012). The spiking component of oscillatory extracellular potentials in the rat hippocampus. J. Neurosci. *32*, 11798–11811.

Siapas, A.G., and Wilson, M.A. (1998). Coordinated interactions between hippocampal ripples and cortical spindles during slow-wave sleep. Neuron *21*, 1123–1128.

Sik, A., Ylinen, A., Penttonen, M., and Buzsáki, G. (1994). Inhibitory CA1-CA3-hilar region feedback in the hippocampus. Science *265*, 1722–1724.

Sirota, A., Csicsvari, J., Buhl, D., and Buzsáki, G. (2003). Communication between neocortex and hippocampus during sleep in rodents. Proc. Natl. Acad. Sci. USA *100*, 2065–2069.

Sullivan, D., Csicsvari, J., Mizuseki, K., Montgomery, S., Diba, K., and Buzsáki, G. (2011). Relationships between hippocampal sharp waves, ripples, and fast gamma oscillation: influence of dentate and entorhinal cortical activity. J. Neurosci. *31*, 8605–8616.

Sun, Y., Nguyen, A.Q., Nguyen, J.P., Le, L., Saur, D., Choi, J., Callaway, E.M., and Xu, X. (2014). Cell-type-specific circuit connectivity of hippocampal CA1 revealed through Cre-dependent rabies tracing. Cell Rep. *7*, 269–280.

Sun, Y., Nitz, D.A., Holmes, T.C., and Xu, X. (2018). Opposing and complementary topographic connectivity gradients revealed by quantitative analysis of canonical and noncanonical hippocampal CA1 inputs. eNeuro *5*, ENEURO.0322-17.2018.

Swaminathan, A., Wichert, I., Schmitz, D., and Maier, N. (2018). Involvement of mossy cells in sharp wave-ripple activity in vitro. Cell Rep. *23*, 2541–2549.

Szabo, G.G., Du, X., Oijala, M., Varga, C., Parent, J.M., and Soltesz, I. (2017). Extended Interneuronal Network of the Dentate Gyrus. Cell Rep. *20*, 1262–1268.

Vinogradova, O.S. (2001). Hippocampus as comparator: role of the two input and two output systems of the hippocampus in selection and registration of information. Hippocampus *11*, 578–598.

Wang, D.V., and Ikemoto, S. (2016). Coordinated interaction between hippocampal sharp-wave ripples and anterior cingulate unit activity. J. Neurosci. *36*, 10663–10672.

Wierzynski, C.M., Lubenov, E.V., Gu, M., and Siapas, A.G. (2009). State-dependent spike-timing relationships between hippocampal and prefrontal circuits during sleep. Neuron *61*, 587–596.

Wilson, M.A., and McNaughton, B.L. (1994). Reactivation of hippocampal ensemble memories during sleep. Science *265*, 676–679.

Wu, C.P., Huang, H.L., Asl, M.N., He, J.W., Gillis, J., Skinner, F.K., and Zhang, L. (2006). Spontaneous rhythmic field potentials of isolated mouse hippocampal-subicular-entorhinal cortices in vitro. J. Physiol. *576*, 457–476.

Xu, X., Sun, Y., Holmes, T.C., and López, A.J. (2016). Noncanonical connections between the subiculum and hippocampal CA1. J. Comp. Neurol. *524*, 3666–3673.

Yamamoto, J., and Tonegawa, S. (2017). Direct medial entorhinal cortex input to hippocampal CA1 is crucial for extended quiet awake replay. Neuron *96*, 217–227.e4.

Ylinen, A., Bragin, A., Nádasdy, Z., Jandó, G., Szabó, I., Sík, A., and Buzsáki, G. (1995). Sharp wave-associated high-frequency oscillation (200 Hz) in the intact hippocampus: network and intracellular mechanisms. J. Neurosci. *15*, 30–46.

STAR★METHODS

KEY RESOURCES TABLE

REAGENT or RESOURCE	SOURCE	IDENTIFIER
Antibodies		
Mouse monoclonal anti-NeuN (1:1000)	Millipore	Cat# MAB377; RRID: AB_2298772
Rabbit monoclonal anti-calbindin (1:10000)	Swant	Cat# CB-38a; RRID: AB_10000340
Goat polyclonal anti-mouse Alexa Fluor 488 (1:500)	ThermoFisher	Cat# A-11029; RRID: AB_2534088
Goat polyclonal anti-rabbit Alexa Fluor 555 (1:500)	ThermoFisher	Cat# A-21429; RRID:AB_2535850
Experimental models: Organisms/strains		
C57BL/6N mice	Charité Central Animal Facility	N/A
Long-Evans rats	Charles River Laboratories	N/A
Software and algorithms		
ImageJ	Schneider et al., 2012	https://imagej.nih.gov/ij/
KiloSort	Pachitariu et al., 2016	https://github.com/cortex-lab/KiloSort
Klusters	Hazan et al., 2006	http://neurosuite.sourceforge.net/
MATLAB R2017b	Mathworks	RRID: SCR_001622
Python version 3.6 and version 3.7	Python Software Foundation	https://www.python.org
Other		
Perforated multi-electrode Array (pMEA) chip	Multi Channel Systems	pMEA32S12-L2
Silicon probes	NeuroNexus	Buzsaki64_8x8

RESOURCE AVAILABILITY

Lead contact

Further information and requests for resources and reagents should be directed to and will be fulfilled by the lead contact, Dietmar Schmitz (dschmitz-office@charite.de).

Materials availability

This study did not generate new unique reagents.

Data and code availability

The datasets/code supporting the current study have not been deposited in a public repository but are available from the corresponding author on request.

EXPERIMENTAL MODEL AND SUBJECT DETAILS

Mice

In vitro experiments were performed on male C57BL/6N mice 3–6 weeks of age. Mice were maintained on a 12-h light / 12-h dark cycle in group cages, with *ad libitum* access to water and standard rodent chow. Animal maintenance and experiments were in accordance with the guidelines of local authorities (Berlin state government, T0100/03, G0151/12) and followed the German animal welfare act and the European Council Directive 2010/63/EU on protection of animals used for experimental and other scientific purposes.

Rats

In vivo experiments were performed on male Long-Evans rats 3–7 months old (350 - 400 g). The rats were maintained on a 12-h light / 12-h dark cycle and were singly housed after implant with *ad libitum* access to water and standard rodent chow. All protocols were approved by the Institutional Animal Care and Use Committee at New York University Langone Medical Center.

METHOD DETAILS

Slice preparation

Mice were decapitated following isoflurane anesthesia. Brains were transferred to ice-cold artificial cerebrospinal fluid (ASCF) slicing solution containing (in mM) 87 NaCl, 50 sucrose, 26 $NaHCO_3$, 10 glucose, 2.5 KCl, 1.25 NaH_2PO_4, 3 $MgCl_2$ and 0.5 $CaCl_2$ (pH 7.4). Horizontal slices of ventral hippocampus were cut on a slicer (VT1200S; Leica) and stored in an interface chamber (32 – 34°C) and perfused with standard ASCF containing (in mM) 119 NaCl, 26 $NaHCO_3$, 10 glucose, 2.5 KCl, 1.0 NaH_2PO_4, 1.3 $MgCl_2$ and 2.5 $CaCl_2$. The slice thickness was 400 μm for patch clamp and LFP recordings and 300-350 μm for MEA recordings.

To study the subicular circuitry in isolation we disconnected the subiculum from CA1 and other parahippocampal areas with a scalpel, under the guidance of a binocular microscope.

The slices used for *in vitro* recordings, where we could systematically observe atypical SWRs, stem from the ventral portion of the hippocampus and they had an approximate interaural distance ranging from 1 to 2.3 mm. The interaural distance was estimated matching the hippocampal structures of recorded slices (either Nissl, calbindin or NeuN stained) with images reconstructed from histological sections from a mouse brain atlas (Franklin and Paxinos, 2007).

The perfusion rate was approximately 1 ml/min. ACSF was equilibrated with carbogen (95% O_2, 5%CO_2). Slices were allowed to recover for at least 1.5 h after preparation.

In vitro electrophysiology

As described previously (Maier et al., 2009), recordings were performed at 31–32°C in a submerged-type recording chamber perfused at high rate (5–6 mL/min).

Multi-electrode array recordings

Simultaneous field recordings from multiple positions were performed with a perforated multi-electrode Array (pMEA) chip (Multi channel Systems, Reutlingen, Germany) equipped with 32 recording and 12 stimulating Titanium nitride (TiN) electrodes. The recording electrodes had a diameter of 30 μm, an impedance ranging from 30 to 50 kΩ and were placed in a 12 × 3 grid (12 columns and 3 rows). The inter-electrode distance (center to center) was 90 μm between columns and 150 μm between rows. The pMEA chip was mounted beneath a small circular recording chamber. Hippocampal slices were carefully positioned on the surface of the pMEA chip so that a large portion of CA1 was covered by the electrode array. The long axis of the pMEA was aligned, as far as the hippocampal curvature allowed, to the stratum pyramidale. A constant negative pressure (5-10 mbar) was applied through the perforation to improve the contact between slices and electrodes. Data were collected with a MEA2100-acquisition system (Multichannel System, Reutlingen, Germany) with a sampling rate of 20 kHz.

Field and patch clamp recordings

For LFP recordings, glass microelectrodes (tip diameter ~5–10 μm; resistance: 0.2–0.3 MΩ) were filled with ACSF before use. Whole-cell recordings were performed with borosilicate glass electrodes (2–5 MΩ) filled with (in mM) 120 K-gluconate, 10 HEPES, 10 KCl, 3 Mg-ATP, 5 EGTA, 2 $MgSO_4$, 0.3 Na-GTP and 14 phosphocreatine. The pH was adjusted to 7.4 with KOH. LFP signals in the CA3 pyramidal cell layer were amplified 1,000-fold, filtered (1–8 kHz), and sampled at 20 kHz. Whole-cell and extracellular recordings were performed using a Multiclamp 700A amplifier (Axon Instruments). For parallel double patch-clamp and field recordings, a custom-made two channel extracellular amplifier was used. Cells were routinely loaded with 0.2% biocytin. After recordings, slices were transferred to 4% paraformaldehyde. Biocytin-filled cells were subsequently visualized with streptavidin conjugated with DyLight 488. After acquisition of confocal images, neuronal reconstruction was performed with the imageJ package (Schneider et al., 2012). To better estimate the slice position along the dorso-ventral axis slices were either Nissl stained or stained with anti-NeuN (Millipore) or anti-calbindin (Swant) antibodies followed by the secondary polyclonal antibody anti-mouse Alexa Fluor 488 or anti-rabbit Alexa Fluor 555 (TermoFisher), respectively.

In vivo juxtacellular recordings

Juxtacellular recordings followed previously described methods (Böhm et al., 2015). Briefly, mice were anaesthetized and implanted with a light-weight metal head holder and a plastic recording chamber centered over the CA1-subicular region. On the day of the experiment, two small craniotomies for local field potential (LFP) and single-cell recordings were made under isoflurane anesthesia (1.5%). For LFP recordings in distal CA1, the glass pipette was inserted at AP 2.5 mm, ML 2.5 mm at 30° angle tilted from the vertical. The glass pipette for juxtacellular recordings was inserted vertically at AP 3 mm, 1.8-2 ML. All *in vivo* signals were amplified with a Multiclamp 700B (Molecular Devices), filtered at 10 kHz, and digitized at 20 kHz (ITC-18; HEKA Elektronik).

In vivo silicon probes recordings

Three rats were implanted with two high-density, 64-channel silicon probes (NeuroNexus) each under isoflurane anesthesia.

Both probes were placed in the left hemisphere above the CA1 area and the subiculum (CA1 transverse axis: 45° angle, centered at AP −4.0 mm, ML 3.0 mm, Subiculum: 90° angle from midline centered at AP −6.8 mm, ML 4.0 mm). During surgery, the tips of the shanks were inserted into the cortex above the respective target. After recovery, the probes were gradually lowered until the

appearance of ripples in each region. Operated animals were housed in individual cages. Experimental sessions were recorded while animals were running on a 1.2 m long linear track as well as in the home cage during the preceding and following resting periods. At the end of the *in vivo* experiments, animals were deeply anesthetized and transcardially perfused with 0.9% saline, followed by 10% formalin in saline. Following an overnight fixation in PFA, brains were washed in PBS before they were mounted on a vibratome and cut into 100 μm slices and counter-stained with DAPI. Signals were acquired using Amplipex at 20 kHz and resampled at 1.25 kHz using a low-pass sinc filter.

QUANTIFICATION AND STATISTICAL ANALYSIS

Data analysis

Data analysis was done using custom-made codes in MATLAB (MathWorks, Natick, MA) and Python 3.6.

Analysis on *in vitro* MEA recordings

Detection of SWRs was performed using a threshold-based algorithm written in MATLAB or Python. The algorithm was carried out on a reference channel with large, positive signals. The ripple peak-times, obtained from the reference channel, were then used to extract a 400 ms stretch of signal for each SWR event from all 32 channels. The extracted signals were centered at the time of ripple peak detected in the reference channel. The extracted signals were subsequently low-pass filtered at 30 Hz and transformed in z-score units. The propagation of SWRs was analyzed using exclusively channels with positive signals, presumably located on or close to the stratum pyramidale. To examine the propagation of SWRs our analysis was limited to channels with a supra-threshold, positive signal. A signal was considered supra-threshold if a minimum threshold of 10 z-scores was reached. To quantify the direction of SWRs propagation the channel was identified where the peak of the z-score transformed signal occurred first. This channel was defined as channel 0 and time 0 was set at its peak-time. The SWR peak-time of the rest of the channels was calculated as time difference from channel 0. The results were always visually verified. To better visualize the direction of propagation of SWRs across all the 32 channels, pseudo-color maps of the z-score of the signals were built in 4 ms time frames during single SWR epochs.

Analysis on *in vitro* field recordings

SWRs detection was performed using a threshold-based algorithm written in MATLAB or Python. After detection, SWR-associated intracellular traces were aligned to the maximum of the local field potential (LFP) ripple and displayed in temporal windows of ± 200 ms from the ripple peak. Spectrograms were constructed using a continuous wavelet transform algorithm applied on stretches of 100 ms of ripple-filtered (150-300 Hz) data centered on the SPW peak. To define the site of origin of each SWR event we employed an algorithm based on comparison between multiple cross-correlations. The cross-correlation were performed on the absolute part of low-pass filtered (< 30Hz) Hilbert transform of ripple-filtered signals. The results were further verified by a careful visual inspection on single event basis. Ripple power was determined by integrating individual PSD functions between 150 and 300 Hz. Ripple duration was defined as the time where the Hilbert transform of the ripple-filtered (150-300 Hz) signal was above 5% of its maximal amplitude. Ripple cycles were calculated as the number of positive peaks for each ripple-filtered SWR. The ripple frequency was calculated by first measuring the inter-ripple interval as ripple duration divided by the number of ripple cycles.

Analysis on *in vitro* patch clamp recordings

To identify SWR-coupled postsynaptic potentials (PSPs) the so obtained voltage (in current-clamp) traces from entorhinal neurons were baseline subtracted and the amplitude of the maximum value was plotted against the peak time (related to SWR peak). The same protocol was carried out for voltage-clamp recordings but the minimum value of the intracellular traces was selected to identify SWR-related postsynaptic inward currents (PSCs). SWR-coupled PSPs were detected as one or two clusters around the SWR peak. Clear clustering of PSP/C-peak time allowed us to distinguish entorhinal cortex (EC)-PSP/Cs following and preceding CA3-SWRs. Based on these criteria the corresponding CA3-SWRs were classified as standard propagating SWRs, if EC-PSP/Cs occurred with a delay, or atypical SWRs if EC-PSP/Cs preceded the CA3-SWR. Careful visual inspection of single traces was additionally performed to exclude that some events were misclassified. EC neurons were considered not to receive any SWR-related synaptic input if no signal was visible in the mean of the 400 ms-long chunked intracellular traces centered at the peak of all SWRs detected in one recording. Onset of subicular- and EC-PSC was defined as the time at which the current deflection crossed 3x the standard deviation of the baseline level. Careful visual inspection was carried out to verify the quality of the detection.

Analysis on *in vivo* recordings

Ripples were detected by running an online available algorithm from the 'buzcode' repository (https://github.com/buzsakilab/buzcode) on one reference channel from the subiculum. The channel with the largest ripple amplitude, defined by visual inspection, was chosen as reference. Briefly, ripples were detected using the normalized squared signal (NSS) by thresholding the baseline. The threshold for ripple beginning/end and ripple peak was set at 2 standard deviations of the NSS, respectively. Ripples were allowed to have a maximum duration of 100 ms. For further analyses, we selected in each shank the electrode with the highest power in the ripple frequency (100-220 Hz) range. From this first selection, we then chose in each shank the channel with the largest ripple power and used the selected channels for further classifying ripples as propagating in a standard (from CA1 to subiculum) or atypical

(subiculum to CA1) fashion. Furthermore, since single event-based analysis can result objectively difficult due to the low signal-to-noise ratio and to the very short delay between signals detected in CA1 and subiculum we filtered out ripples which did not achieve, both in the reference CA1 and subiculum channels, a value at least as twice as large as the standard deviation calculated outside ripple periods.

For classifying the filtered ripples as standard or potentially atypical we employed a semi-automatic algorithm based on a combination of onset and cross-correlation peak-times. The algorithm ran on 500 ms stretches of ripple-filtered (100-220 Hz) signal centered on the ripple peak. The results were further verified by a careful visual inspection on single event basis. To compute the spectrograms of the signal we employed a continuous wavelet transform algorithm applied on stretches of 100 ms of ripple-filtered (100-220 Hz) signal centered on the ripple peak. Analysis on spikes were conducted on sessions where more than three atypical ripples could be detected. Spike clusters were extracted from the high-passed filtered signal using KiloSort (Pachitariu et al., 2016); a manual curating step, where units were merged based on common refractoriness and waveform similarity was performed using Klusters (Hazan et al., 2006). Units significantly positively modulated by ripples were included in the raster plots.

Statistics

To compare ripple frequency, the number of ripple cycles, ripple duration and the ripple power as well as to compare the portion of atypical SWRs before and after cutting the EC we employed the paired t test after verification of normality with the Kolmogorov-Smirnov test. To compare the time of firing of CA1 neurons during standard and atypical ripples in the *in vivo* recordings we employed the Mann-Whitney U test after we verified with the Kolmogorov-Smirnov test that the data were not normally distributed. Results are presented as mean ± standard error of the mean (SEM).

P values below 0.05 were regarded as statistically significant. One, two or three asterisks, if used in graphs, indicate p values between < 0.05 and 0.01, < 0.01 and 0.001 and < 0.001, respectively.